Effect of rake angle on strain field during orthogonal cutting of hardened steel with c-BN tools

Thomas Baizeau[a,*], Sébastien Campocasso[a,b], Guillaume Fromentin[a], Frédéric Rossi[a], Gérard Poulachon[a]

[a]*Arts et Metiers ParisTech, LaBoMaP, Rue Porte de Paris, 71250 Cluny, France*
[b]*CEA, DAM, Valduc, 21120 Is-sur-Tille, France*

Corresponding author. Tel.: +003-385-595-344. *E-mail address:* thomas.baizeau@ensam.eu

Abstract

In the case of hard machining of steels, negative rake tools generate compressive deformation and high temperature under the cutting edge, leading to phase transformation or "white layers". The resulting surface integrity can be predicted by numerical simulations which may be validated by comparing simulated and measured strain fields. Recent high speed imaging devices have facilitated strain field measurement by Digital Image Correlation (DIC), even at high strain rates. However, the analyse is generally restricted to the primary shear zone and not to the workpiece under the machined surface. For this study, a double-frame camera and a pulsed Nd:YAG laser, generally used in the field of fluid mechanics, have been employed to record images during an orthogonal cutting operation of a hardened steel. The effect of the rake angle and the edge preparation of c-BN tools on the subsurface displacement field, which has been experimentally investigated by using DIC, are presented in this paper together with an analysis on the origins of the strains. The results of these measurements will be used to validate cutting numerical simulations or to improve hybrid modelling of surface integrity.

1. Introduction

During machining of hardened steels, the extreme conditions of temperature and stress may lead to phase transformation. In order to predict the surface integrity of the machined part, recent research works have developed more and more complex models of the cutting operations. Chou and Evans [1] used an analytical approach of moving heat source on workpiece to simulate "white layer" formation. Movahhedy *et al.* proposed a Johnson-Cook based finite element modelling in order to determine stress, strain and temperature induced by hard cutting of P20 grade steel [2]. After characterising the "white layer" generated during hard AISI 52100 steel machining [3], Ramesh and Melkote added a phase transformation law and the induced plasticity in a FEM simulation based on Johnson-Cook material law [4]. Umbrello *et al.* proposed an empirical modelling of the "white" and "black" layers formation implemented also in a FEM modelling [5,6]. However, these models are based on material constitutive laws identified at lower strain rates and temperatures than these found in the primary (PSZ), secondary (SSZ) and tertiary (TSZ) shear zones. Moreover, material law parameters are generally identified by comparing simulated and measured macroscopic outputs like cutting forces, chip morphology or tool/chip contact length. Unfortunately, few experimental datas of the inner part of the workpiece have been collected, whereas the part life time is mainly due to the surface integrity.

Historically, chip formation mechanisms were analysed by post-mortem observations, as it had been investigated by Poulachon and Moisan [7] in the case of hard turning by using quick stop tests (QST). Consequently geometrical parameters such as shear plane angle Φ_s or chip thickness h_c can be determined. Strains and strain rates can be estimated by analysing the grain deformations on micrographs when the grain size is coarse enough. Although this technique can be performed during 3D cutting, it is quite hasardous, time consuming and the strain remains only estimated.

In order to measure the strains, the distortion of some markers must be followed. These markers are not limited to the micro-structure or the roughness of the observed surface, and can also be found under different shapes like grids, lines, pads or stains, added or removed to the specimen. These preparations can be performed for instance by lithography printing, spray painting, etching, EDM, micro-blasting or abrasion in or-

der to provide a suitable texture to the observed surface, that will be transform into grey levels by an imaging device.

Thanks to the development of high performance optical sensors in terms of sensibility, frame rate, exposure time, resolution and noise, high speed imaging devices are now operable for recording images of cutting operations at commonly used conditions of cutting speed V_c and uncut chip thickness h. However, to get accurate measurements with correct spatial resolutions of the strain field, the experimental environment and the full acquisition device employed are also critical.

Among previous works, Pujana *et al.* [8] applied a square grid marking on a 42 CrMo 4 specimen to analyse the PSZ during the cutting process at $V_c = 150$ and 300 m.min^{-1}, with a recording rate of 25,000 fps and an exposure time of 8 µs, corresponding to an inter-framing displacement of 8 % of the grid size at the employed speeds. List *et al.* [9] worked on AISI 1040 steel with a line marked surface at $V_c = 1,020$ m.min^{-1} on a ballistic apparatus, but with an overdone uncut chip thickness of 0.63 mm to get enough lines in the PSZ. The revealed micro-structure was used by Pottier *et al.* [10] to study a Ti6Al4V at a low cutting speed $V_c = 6$ m.min^{-1} , and by Hijazi and Madhavan [11] for a 42 CrMo 4 at $V_c = 300$ m.min^{-1} and $h = 0.1$ mm. An experimental configuration of fixed tool and moving specimen is commonly used, leading in the case of Arriola *et al.* [12] to blurred pictures at $V_c = 300$ m.min^{-1} due to the 1.8 µs time exposure. Hijazi and Madhavan [11] employed simultaneously four double pulsed lasers with a complex optical beam splitter to light up four double-frame imagers. By working in the dark, the 5 ns laser pulse duration enable to compensate the high exposure time of the used imagers leading to sharp final images. In spite of the quality of the experimental devices used, observation of hardened steel cutting with negative c-BN tools by high speed imaging has not been reported yet.

Concerning the image analysis, it can be done either by grid or line tracking [8,9] or by digital image correlation (DIC) [10–12]. The DIC consists in recording at least two pictures I and J of the same scene taken at different times and then in determining the displacement field $\underline{U}$ that best fits to minimise over a region of interest (ROI) – decomposed in elementary zone of interest (ZOI) – the residual grey level of each ZOI estimated by $\tau_{Local\ DIC}$ in the case of a local DIC approach (Eq. (1)) and the global residual grey level $\tau_{Global\ DIC}$ in the case of a global approach [13], given at Eq. (2).

$$\tau_{Local\ DIC} = \int_{ZOI} \left[I(\underline{x}) - J\left(\underline{x} + \underline{U}(\underline{x})\right) \right]^2 d\underline{x} \quad (1)$$

$$\tau_{Global\ DIC} = \int_{ROI} \left[I(\underline{x}) - J\left(\underline{x} + \underline{U}(\underline{x})\right) \right]^2 d\underline{x} \quad (2)$$

$$\text{with} \quad \underline{U} = \sum \underline{U}_e \cdot \psi_e(\underline{x})$$

Most of the strain field measurements realised when machining employed local approaches that consider each ZOI independent from the others and allow them to overlap or to be separate. In the case of a global approach, the displacements are estimated on a continuous mesh that satisfied the continuity between elements. In both case, displacements are estimated by shape functions ψ, but as Hild and Roux [14] reported in their comparison between local and global approaches, the global one allows using finer meshing and thus leads to a higher resolution. More complex displacement fields can be captured and the displacement determination is more robust to noise than the local one. Besides, this FE-based global approach can also be directly linked to numerical simulations without any interpolation of the measured displacements. For all of these reasons, a Q4P1 shape function based on global DIC approach has been chosen for the present study, concerning the displacement field measurement during orthogonal cutting of a 100 CrMo 7 hardened steel with negative c-BN tools.

After detailing the experimental set-up, some global conclusions on the experimental work are given. Then, the effect of the cutting edge geometry on the displacement field in the workpiece is investigated and compared to an elastic finite element simulation. Finally, a comparison between post-mortem analysis and *in-situ* measured strains is proposed regarding the plastically deformed layer under the machined surface.

2. Experimental set-up

2.1. Acquisition device

The planing operation has been performed along the x-axis of a DMG DMC85V 3-axis milling machine, having linear motors that enable a translation speed up to 120 m.min^{-1}. A gradual acceleration has been performed by a speed loop-back command in order to reach the targeted cutting speed few millimetres before entering material. The side of the specimen has been observed by a LaVision sCMOS double-frame imager with a x10 Mitutoyo telecentric objective providing a spatial resolution of 0.66 µm.px^{-1} on the 2560x2160 pixels sCMOS sensor encoded on 16 bits (65536 grey levels). Pictures pairs composed of two frames (f_0 and f_1) can be recorded at 15 Hz with an adjustable inter-framing time dt_{if} from 120 ns to 30 ms and a minimal exposure time of 10 ms. To get non-blurred images, the scene has been lightened by a compact dual-cavity pulsed Nd:YAG 30 mJ laser head (Litron NS 30-15). Each laser performs a 5 ns flash – giving the effective exposure time – delayed by dt_{if} and with a beam diameter of 3 mm. A liquid light guide ended by an expander is employed to homogeneously lighten the scene with a spot diameter around 30 mm. The laser head and the imager are synchronised by the programmable timing unit (PTU) and the LaVision Davies software in order to enlighten the frame f_0 with the laser L1 and the frame f_1 with the laser L2.

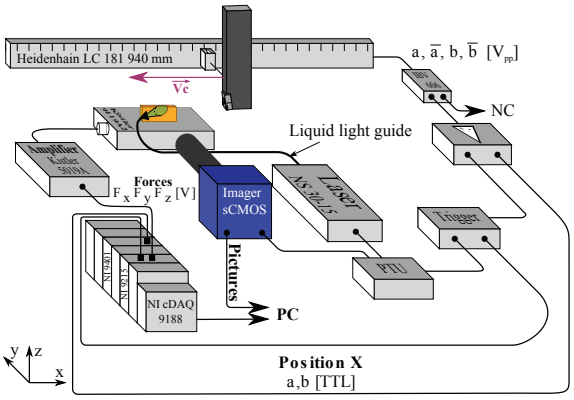

Fig. 1: Principle of the experimental set-up.

Based on the incremental signal counting – by a dedicate micro-controller – of the x-linear encoder, an advanced triggering system has been specially developed to capture the cutting tool in the 1.7x1.4 mm observed field. The current position of the tool is compare to the targeted set position with a 187.5 kHz refresh rate. With the Heidenhain IBV-606 interpolation (x2) of the 16 µm V_{pp} sinusoidal signals, the final spatial resolution of the TTL quadrature signals is 8 µm, while the maximal cutting speed reachable corresponds to $V_c = 90$ m.min^{-1}. A logical gate comparator is plugging between the encoder and the trigger to clean a and b noisy signals with their respective conjugated $\bar{a}$ and $\bar{b}$ signals, as shown in Fig. 1.

During the experimentations, cutting forces F_x, F_y and F_z have been monitored by a Kistler 9119AA2 piezoelectric dynamometer and its charge amplifier (Kistler 5019A). Thanks to a NI cDAQ-9188 acquisition device, NI 9215 analogic and NI 9401 digital counting acquisition cards, once the cutting forces, the triggering signal of the PTU and the x-position have been recorded synchronously with the same clocktime allowing to know F_x, F_y, F_z, x and V_c at the exact time of the picture pair during the cutting. Two other picture pairs have been also recorded: one before the cut and one after. A total of three pairs (*i.e.* 6 frames) have been recorded for each cutting test:

- 1 pair before the cutting test: $P1_{\{f_0,f_1\}}$;
- 1 pair during the cutting: $P2_{\{f_0,f_1\}}$;
- 1 pair after: $P3_{\{f_0,f_1\}}$

2.2. Tool and machined specimen

The specimen material used for this study is a 56 HRC_{150} hardened 100 CrMo 7 bearing steel in conformity with the ISO 6083-17:2001 standard according to mass spectrometer analysis realised. The 35x15x2.5 mm specimens have been extracted in hardened tubes obtained by 850°C austenitising, hot oil quenching and 110°C tempering during 60 minutes. The material presents ultra-fine carbides in a 60 % martensitic and 40 % bainitic structure with an average grain size of 5 µm.The extraction of the specimens has been performed by wire EDM cutting giving a particular roughness to the surfaces subsequently used for the DIC. A 45°x3 mm chamfer has been grind to reduce shocks at the entrance of the tool during the cut of the 35 mm long specimen. A measurement of the textured surface has been done with an optical interferometer Veeco Wyko NT1100 with a x5 objective. After a 0.25 mm Lc Gaussian filtering, the surface presents an arithmetical mean height $S_a = 1.2$ µm, a peak density $S_{pd} = 436$ peak.mm^{-2} and a mean peak curvature $S_{pc} = 501$ mm^{-1}, without any anisotropy.

Based on this texture, the obtained images have a grey level repartition over 2^{10} bits as presented in Fig. 2 and permit a 12x12 px element size correlation (7.68x7.68 µm), according to the correlation radius and the mean fluctuation criterion defined by Besnard *et al.* [13].

To study the effect of the cutting edge on strain field, four geometrically different tools with identical c-BN grade inserts have been employed. The Arno AH7510 grade is a polycrystalline c-BN grade with high c-BN content, fine-grained structure and metallic binder. A specific tool holder has been designed to ensure orthogonal cutting conditions ($\kappa_r = 90°$ and $\lambda_s = 0°$) and a clearance angle $\alpha_n = 7°$. The characteristics of each tool are presented in Table 1. Every tool corners have

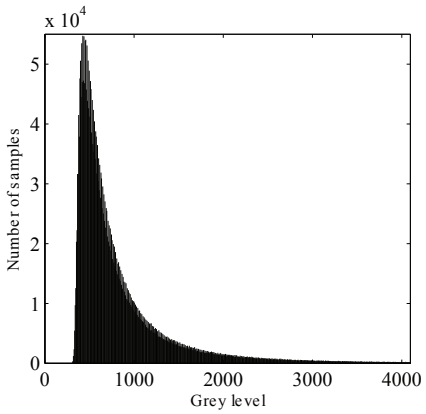

Fig. 2: Grey-level distribution.

been grinded in order to guarantee that the cut is performed on the linear part of the major cutting edge as shown in Fig. 3. Also employing a grinded tool allows to contain both the tool and the specimen in the depth of focus leading to a precise observation. As $\lambda_s = 0°$, the width of cut b is equal to the specimen thickness ($b = 2.5$ mm) and has been chosen to be less than the remaining c-BN cutting edge insert after grinding. Finally, the uncut chip thickness h is set with the z axis translation of the machine-tool.

Table 1: Cutting tool characteristics.

Tool number	Tool reference	Effective rake angle γ_n (°)	Edge prep.
T1 & T2	CCGW060202 FN	0	Honed
T3 & T4	CCGW060202 TN	-20	Chamfered
T5 & T6	CNGA120408 FN	-7	Honed
T7 & T8	CNGA120408 TN	-27	Chamfered

Due to the experimental configuration, all tests have been performed at $V_c = 90$ m.min^{-1} with an inter-frame time $dt_{if} = 10$ µs corresponding to 15 µm displacement between each frame. Three levels of h (0.05, 0.1 and 0.15 mm) have been tested and repeated three time.

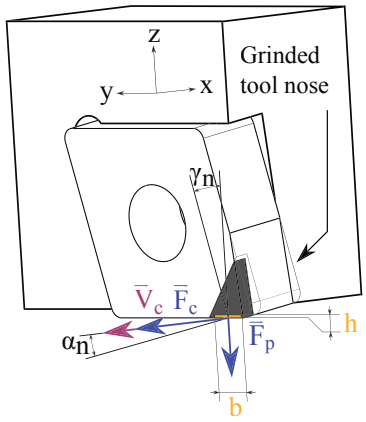

Fig. 3: Cutting tool holder and insert.

3. Global analysis

3.1. Chip analysis and tool behaviour

Chip morphologies and shear plane angles obtained for each rake angle γ_n and each uncut chip thickness h are shown in Table 2. It appears that the cut is well performed in terms of chip morphology – with curled and serrated chips – when the cutting tool has a rake angle γ_n between -20° and -7°. During the tests with $\gamma_n = 0°$, a catastrophic failure of the cutting edge appeared for both tools T1 and T2 in spite of the entering chamfer of the workpiece. Furthermore, formed chips are continuous without localised shearing bands as expected in the case of hard-machining. In the case of $\gamma_n = -27°$, the chip did not flow along the rake face but at both sides of the specimen, leading to significant burrs.

By performing digital image correlation between the two frames of the pair acquired during the cut ($P2_{f_0}$ and $P2_{f_1}$), the shear plane angle is measured. In the case of $h = 0.1$ mm and $\gamma_n = -7°$ configuration, Φ_s is around 43°± 0.7°.

Table 2: Chip morphology.

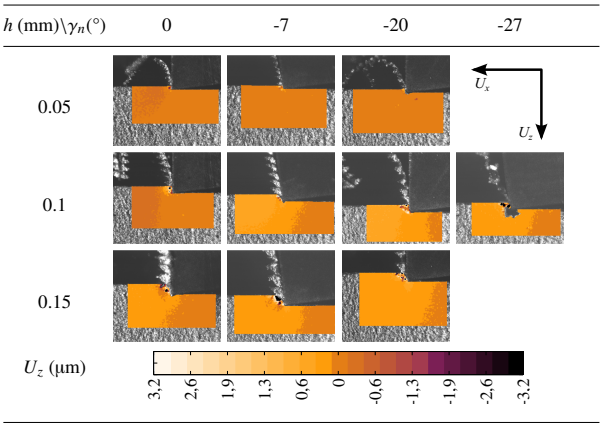

3.2. Cutting force modelling

A mechanistic cutting force model allowing as simply as possible to represent the experimental measurements [15] has been chosen. Two linear forces, denoted $\vec{f_c}$ and $\vec{f_p}$ respectively collinear to $\vec{V_c}$ and orthogonal to the cutting edge in the plane P_r, are determined with respect to h as shown in Eq. 3. The cutting coefficients K_{ci} and k_{ei} are commonly analysed as being respectively the effect of the cutting process by shearing and the edge effect [16].

$$\begin{cases} f_c &= K_{cc} \cdot h + k_{ec} \\ f_p &= K_{cp} \cdot h + k_{ep} \end{cases} \quad (3)$$

For each tool, the values of the cutting coefficients, given in Tables 3 and 4, are identified by minimising the sum of squared deviations between the measured forces $f_{i_{mes}}$ and the modelled forces $f_{i_{mod}}$. The orthogonal cutting configuration leads to $f_c = F_c/b = F_x/b$ for the cutting component and $f_p = F_p/b = F_z/b$ for the thrust force.

Table 3: Identified coefficients for the cutting force f_c with the maximal relative error RE_{max} and the mean relative error RE_{mean}.

γ_n (°)	K_{cc} ($N.mm^{-2}$)	k_{ec} ($N.mm^{-1}$)	RE_{max} (%)	RE_{mean} (%)
0	2804	40	8.7	4.7
-7	2445	77	5.5	1.5
-20	2077	101	6.8	2.1
-27	2520	11	11.7	3.8

Table 4: Identified coefficients for the thrust force f_p with the maximal relative error RE_{max} and the mean relative error RE_{mean}.

γ_n (°)	K_{cp} ($N.mm^{-2}$)	k_{ep} ($N.mm^{-1}$)	RE_{max} (%)	RE_{mean} (%)
0	1114	64	10.3	6.4
-7	782	122	2.5	1.1
-20	1024	136	8.1	3.9
-27	1206	218	9.4	4.1

The obtained values of the shear plane angle, the specific cutting force and specific thrust force will be employed as inputs in the elastic-FE model presented in section 4.2.

4. Field analysis

As explained in section 1, the displacement fields in the specimen have been measured by using a global DIC analysis realised by Correli^{Q4} software (developed in LMT Cachan laboratory, France). After subtracting the predetermined rigid body motion (RBM) induced by the system stiffness, U_x and U_z displacement fields have been plotted.

4.1. Displacement fields

The displacement fields measured between the pictures taken before and during the cut, $P1_{f_0}$ and $P2_{f_0}$, are shown in Tables 5 and 6 for respectively x and z direction. An important outcome of these measurements is that the in-depth deformations are mainly due to the PSZ.

Table 5: U_x displacement fields between $P1_{f_0}$ and $P2_{f_0}$.

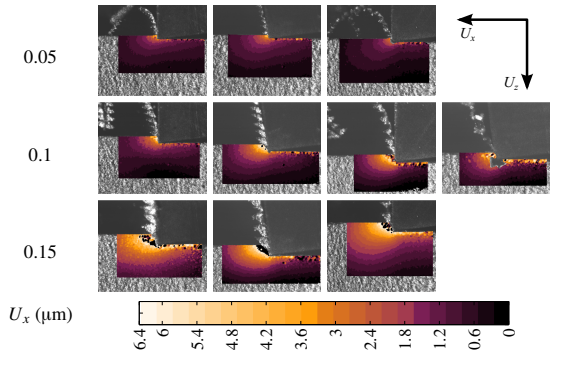

Table 6: U_z displacement fields between $P1_{f_0}$ and $P2_{f_0}$.

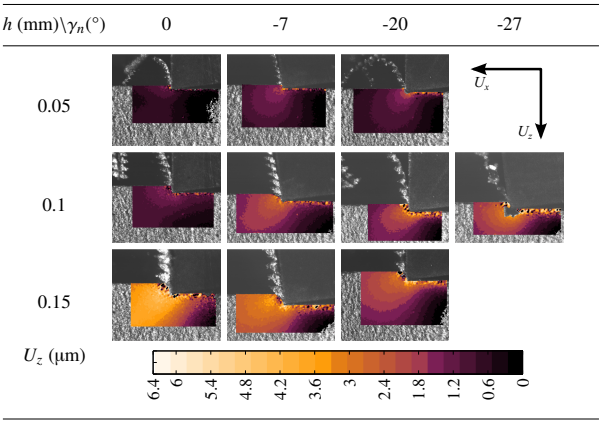

Also according to these results, the rake angle seems to have less influence both on the shape and the amplitude of the displacement fields than the uncut chip thickness. Raising h increases the total deformation depth and the amplitude of the displacements. Furthermore, the newly generated surface presents a highly deformed layer whose thickness increases when the rake angle decreases or the uncut chip thickness increases.

As the displacement determination has been done in a loaded situation – the tool is cutting –, the measured displacements are resulting from both elastic and plastic deformations. The smooth and regular shape of the fields in depth could result from the cumulation of the elastic deformations, whereas the chaotic part could be mainly due to the plastic deformations. In order to confirm these assumptions, a simplified elastic model is proposed and discussed in the next subsection.

4.2. Elastic FE-Modelling

In order to validate both the shape and the amplitude of the measured displacements, a simplified elastic finite element model has been realised. The specimen has been modelled as presented in Fig. 4, with x and z translations blocked at the bottom. According to the linear cutting force f_c and the thrust force f_p modelled in section 3.2, equivalent pressures K_{cc} and K_{cp}, respectively oriented in x and z directions and representing the cutting load have been applied on a surface assumed to be the PSZ. The shear plane has been inclined by the shear plane angle Φ_s estimated to be around 43° in section 3.1. The results for the studied case ($h = 0.1$ mm and $\gamma_n = -7°$) are presented in Fig. 5.

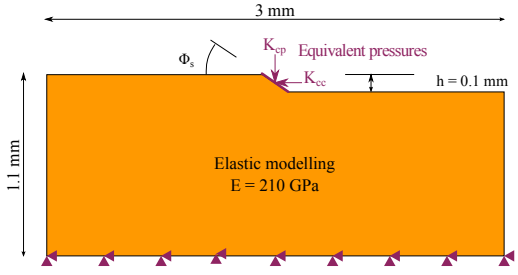

Fig. 4: Elastic finite element modelling representation.

The general shapes of both displacement fields are confirming the measured ones. Moreover, the amplitudes are in agreement and bring the conclusion to an in-depth elastic displacement field.

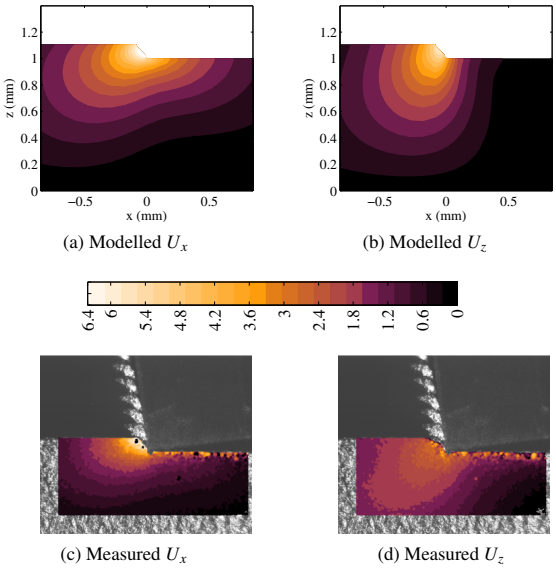

(a) Modelled U_x (b) Modelled U_z

(c) Measured U_x (d) Measured U_z

Fig. 5: Displacement fields simulated by elastic modelling along: (a) x-direction; (b) z-direction; measured along: (c) x-direction; (d) z-direction, for $h = 0.1$ mm, $\gamma_n = -7°$.

4.3. Plastically deformed layer

The subsurfacic layer presenting a tumultuous displacement field, described in section 4.1, can be compared to the plastically deformed layer induced by the cutting operation. To do so, a measured displacement field between $P1_{f_0}$ and $P3_{f_0}$- is compared to the deformed layer observed on micrographs prepared on the side surface and in a cross section of the specimen by polishing and a 5 s nital etching. For the case study specimen ($h = 0.1$ mm and $\gamma_n = -7°$), the thickness of the deformed layer has been measured in ten different points and the mean values are compared in Tables 7 and 8. Unfortunately, the estimation of the thin deformed layer thickness by micrographic analysis is highly linked to the observer accuracy and the results need to be confirm by quantitative techniques like EBSD [17]. With the DIC, a sharp layer delimitation is obtained and has the same thickness by analysing x or z displacement. Finally, the DIC-determined thickness is near to the one obtained by the cut view, showing the capability of the technique for measuring the plastically deformed layer. Nonetheless, this deformed layer does not correspond to the so-called "white layer" which has not been observed in the present case.

5. Conclusion

This paper presents some of the difficulties encountered during the cutting process study either by post-mortem analysing or by in-situ imaging of the cutting operation. Sharp images have been obtained by an advanced experimental set-up using a

Table 7: Measurement of the plastically deformed layer by DIC.

	U_x by DIC	U_z by DIC
Fields	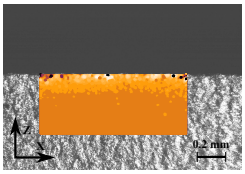	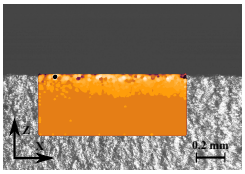
Layer thickness	49 µm	50 µm

Table 8: Measurement of the plastically deformed layer by optical observation.

	Side view	Cut view
Picture	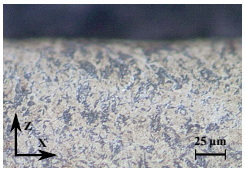	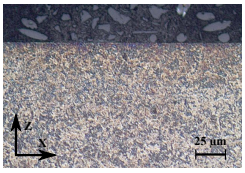
Layer thickness	21 µm	52 µm

pulsed laser lighting for very low exposure time and a high performance triggering device. A numerical post-processing has been performed by a global digital image correlation approach that allows the measurement of the displacement fields and the calculation of the strain fields. This work provides experimental evidence of cutting edge geometric effect on the cutting forces and the displacement fields in the workpiece.

In one hand, from an industrial point of view, only the honed and chamfered ($-20°$) $\gamma_n = 0°$ tool or the simply honed $\gamma_n = -7°$ tool can produce correct cutting conditions. Furthermore, it has been shown that the plastically deformed layer is influenced by both the cutting edge preparation and the tool holder geometry. In the other hand, the DIC analysis before and during cutting has shown the cumulative displacements induced by the hardly measurable elastic strains, as substantiated by the FE simulation, while analysing "before-after" cutting images offers an easy and robust determination procedure of the plastically deformed layer.

In the near future, the DIC results will be compared to multi-physics modelling of the cutting process, especially concerning the residual deformed layer. Also, fine analysis of the measurement uncertainty and the repeatability of the measured fields are needed to ensure the suggested approach. Another outlook of this work could be to improve DIC calculation by employing closer displacement shape functions than Q4 one. Finally, a full validation of a complex multi-physics model will need further works on temperature field measurement for instance.

Acknowledgements

The authors gratefully thank:

- the ADEME for the financial support through the Wind-Process project;
- NTN-SNR for the material support;
- the CEA Valduc for providing the imaging device.

References

[1] Chou, Y., Evans, C.J.. White layers and thermal modeling of hard turned surfaces. International Journal of Machine Tools and Manufacture 1999;39(12):1863 – 1881.

[2] Movahhedy, M., Altintas, Y., Gadala, M.. Numerical analysis of metal cutting with chamfered and blunt tools. Journal of Manufacturing Science and Engineering 2002;124(2):178–188.

[3] Ramesh, A., Melkote, S., Allard, L., Riester, L., Watkins, T.. Analysis of white layers formed in hard turning of aisi 52100 steel. Materials Science and Engineering 2005;390(1–2):88–97.

[4] Ramesh, A., Melkote, S.N.. Modeling of white layer formation under thermally dominant conditions in orthogonal machining of hardened aisi 52100 steel. International Journal of Machine Tools & Manufacture 2008;48(3–4):402–414.

[5] Umbrello, D., Filice, L.. Improving surface integrity in orthogonal machining of hardened aisi 52100 steel by modeling white and dark layers formation. CIRP Annals - Manufacturing Technology 2009;58(1):73–76.

[6] Umbrello, D., Jayal, A., Caruso, S., Dillon, O., Jawahir, I.. Modeling of white and dark layer formation in hard machining of aisi 52100 bearing steel. Machining Science and Technology 2010;14(1):128–147.

[7] Poulachon, G., Moisan, A.. Hard turning: Chip formation mechanisms and metallurgical aspects. Journal of Manufacturing Science and Engineering 2000;122(3):406–412.

[8] Pujana, J., Arrazola, P., Villar, J.. In-process high-speed photography applied to orthogonal turning. Journal of Materials Processing Technology 2008;202(13):475 – 485.

[9] List, G., Sutter, G., Bi, X., Molinari, A., Bouthiche, A.. Strain, strain rate and velocity fields determination at very high cutting speed. Journal of Materials Processing Technology 2013;213(5):693 – 699.

[10] Pottier, T., Germain, G., Calamaz, M., Morel, A., Coupard, D.. Sub-millimeter measurement of finite strains at cutting tool tip vicinity. Experimental Mechanics 2014;54(6):1031–1042.

[11] Hijazi, A., Madhavan, V.. A novel ultra-high speed camera for digital image processing applications. Measurement Science and Technology 2008;19(8):085503.

[12] Arriola, I., Whitenton, E., Heigel, J., Arrazola, P.. Relationship between machinability index and in-process parameters during orthogonal cutting of steels. CIRP Annals - Manufacturing Technology 2011;60(1):93–96.

[13] Besnard, G., Hild, F., Roux, S.. Finite-element displacement fields analysis from digital images: Application to portevinle chatelier bands. Experimental Mechanics 2006;46(6):789–803.

[14] Hild, F., Roux, S.. Comparison of local and global approaches to digital image correlation. Experimental Mechanics 2012;52(9):1503–1519.

[15] Armarego, E.J.A., Epp, C.J.. An investigation of zero helix peripheral up-milling. International Journal of Machine Tool Design and Research 1970;10(2):273–291.

[16] Armarego, E.J.A., Whitfield, R.C.. Computer based modelling of popular machining operations for force and power prediction. CIRP Annals - Manufacturing Technology 1985;34(1):65–69.

[17] M'Saoubi, R., Axinte, D., Herbert, C., Hardy, M., Salmon, P.. Surface integrity of nickel-based alloys subjected to severe plastic deformation by abusive drilling. CIRP Annals - Manufacturing Technology 2014;63(1):61–64.